

ARTICLE

Received 12 Mar 2013 | Accepted 31 May 2013 | Published 27 Jun 2013

DOI: 10.1038/ncomms3077

OPEN

Integrated Mach-Zehnder interferometer for Bose-Einstein condensates

T. Berrada¹, S. van Frank¹, R. Bücke¹, T. Schumm¹, J.-F. Schaff¹ & J. Schmiedmayer¹

Particle-wave duality enables the construction of interferometers for matter waves, which complement optical interferometers in precision measurement devices. This requires the development of atom-optics analogues to beam splitters, phase shifters and recombiners. Integrating these elements into a single device has been a long-standing goal. Here we demonstrate a full Mach-Zehnder sequence with trapped Bose-Einstein condensates confined on an atom chip. Particle interactions in our Bose-Einstein condensate matter waves lead to a nonlinearity, absent in photon optics. We exploit it to generate a non-classical state having reduced number fluctuations inside the interferometer. Making use of spatially separated wave packets, a controlled phase shift is applied and read out by a non-adiabatic matter-wave recombiner. We demonstrate coherence times a factor of three beyond what is expected for coherent states, highlighting the potential of entanglement as a resource for metrology. Our results pave the way for integrated quantum-enhanced matter-wave sensors.

¹Vienna Center for Quantum Science and Technology, Atominstitut, TU Wien, Stadionallee 2, 1020 Vienna, Austria. Correspondence and requests for materials should be addressed to J.-F.S. (email: jschaff@ati.ac.at).

Atom interferometers¹ are powerful tools for a wide variety of measurements. They have been used to measure atomic properties², to study quantum degenerate systems^{3,4}, for precision measurements⁵, and are very sensitive probes for inertial effects⁶, as beautifully demonstrated, for example, in gravimeters⁷ and gyroscopes⁸.

Whereas interferometers with atoms propagating in free fall are ideally suited for inertial and precision measurements^{5–9}, interferometers where the atoms are held in tight traps or guides are better for measuring weak localized interactions, as, for example, proposed to probe the Casimir–Polder force¹⁰.

In most atom interferometers to date, the matter waves propagate freely and the two interfering arms correspond to wave packets having different momenta¹. The beam splitters creating the superposition either couple different internal states, like in the Raman beam splitter, or leave the matter wave in the same atomic state, like in Bragg scattering or diffraction from a material grating.

Bose–Einstein condensates (BECs) are promising candidates for atom interferometry owing to their macroscopic coherence properties^{11–14}. Following the first observation of BEC interference in 1997 (ref. 11), various building blocks of BEC interferometers have been realized individually. Interference experiments with BECs were performed using Bragg beams in ballistic expansion¹², with atoms freely propagating in a guide^{15,16}, and very recently under microgravity¹⁷. Splitting a single trapped BEC into two separated clouds in a double

well, interference was observed using ballistic expansion after switching off the trapping potential^{18–22}. Realizing a full Mach–Zehnder interferometer with spatially separated modes of trapped BECs has been a long-standing goal^{23–25}, especially in chip traps, where the tight confinement allows local probing.

A fundamental difference between photon and matter-wave optics is the presence of atom–atom interactions. In dense, confined geometries they lead to dephasing (phase diffusion), which ultimately limits the coherence time of the interferometers^{22,26–28}. Phase diffusion can be reduced by controlling the interactions with a Feshbach resonance. Coherence times up to 10 s were recently demonstrated in Bloch oscillation experiments^{29,30}.

Interactions can also be used to generate non-classical correlations between the two paths of the interferometer, which can be used either to improve the sensitivity³¹ or to reduce the effect of phase diffusion²⁰. Generation of entanglement was recently reported for BECs in multiple-well potentials³², and between two or three internal states of spinor BECs^{33–37}. In Gross *et al.*³³, entanglement was used in an internal state BEC interferometer to improve its sensitivity below the standard quantum limit $\delta\phi_{\text{SQL}} = 1/\sqrt{N}$, where N is the number of atoms involved in the measurement.

Here, we demonstrate a full Mach–Zehnder interferometer for BECs integrated on an atom chip. Our interferometric scheme relies on the coherent splitting and recombination of a BEC in a tunable magnetic double-well potential, where the matter wave is

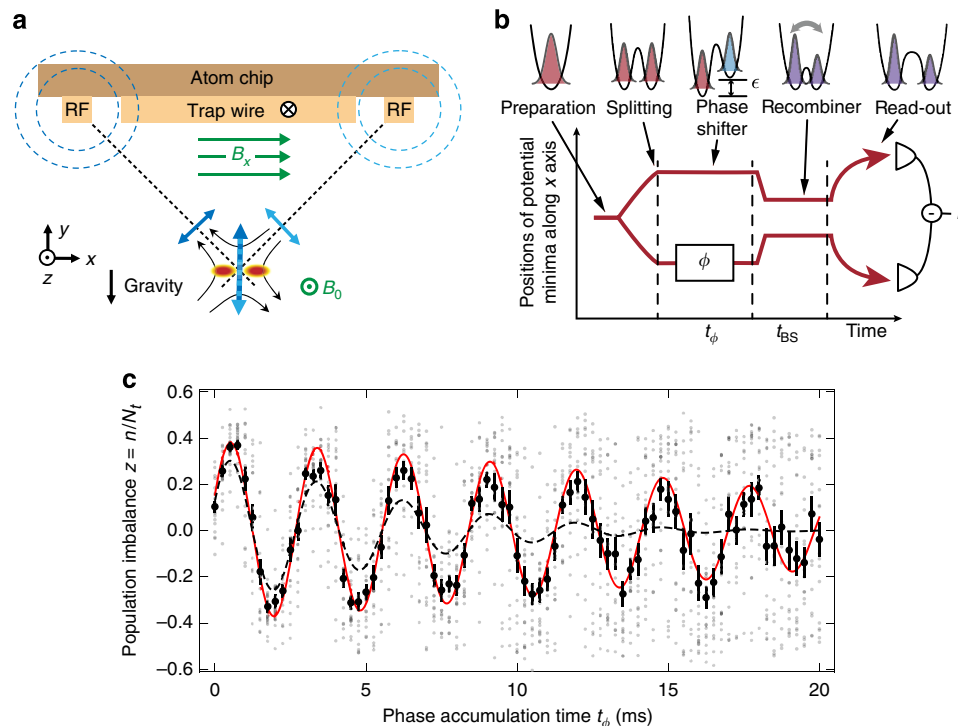


Figure 1 | The Mach–Zehnder interferometer and its output signal. (a) Schematic of the atom chip: a DC current of 1 A is sent through the trap wire, which, together with a uniform external ‘bias’ field $B_x = 29.5$ G, creates an elongated quadrupole trap $60 \mu\text{m}$ below the chip. The longitudinal confinement is realized by two wires parallel to the x axis (not shown here). An external field B_0 completes the Ioffe–Pritchard configuration. Rf currents with a relative phase of π are applied on the dressing wires to perform the splitting along x . (b) The condensate is coherently split by transforming a single trap into a double-well potential; a relative phase between the two arms is imprinted by tilting the double well during a time t_ϕ ; the spacing between the two wells is then abruptly reduced and the potential barrier acts as a beam splitter for both wave packets, transforming the relative phase into a population imbalance. After the recombination time t_{BS} , the atom clouds are separated and the particle number in each well is read out by fluorescence imaging. (c) The normalized population difference between the two wells $z = n/N_t$ is measured as a function of t_ϕ . It exhibits interference fringes and a damping due to phase diffusion. Grey dots: imbalance of individual experimental realizations; black dots: ensemble average $\langle z \rangle$; red curve: theoretical prediction taking into account phase diffusion; dashed black line: expected signal for a classical coherent state for which $\xi_N = 1$. The error bars indicate ± 1 s.e.m.

confined at all times. Thanks to a spatial separation of $\sim 2 \mu\text{m}$ between the two wave packets, our geometry is sensitive to accelerations and rotations. By tilting the double well out of the horizontal plane for a variable time t_ϕ , we apply an energy difference ϵ and thereby imprint a controlled relative phase between the interferometer arms. A non-adiabatic recombiner translates the relative phase into an atom number difference, which is directly read out using a highly sensitive time-of-flight fluorescence detector³⁸. We show that the use of a non-classical state with reduced number fluctuations inside the interferometer helps increasing the interrogation time, which is still limited by interaction-induced dephasing. This represents an unambiguous demonstration of the interplay between number fluctuations and phase diffusion in the case of spatially separated modes of BECs.

Results

Principle and interferometric fringes. The atom chip used to manipulate the atomic wave packets is depicted in Fig. 1a. The interferometer sequence is illustrated in Fig. 1b, and Fig. 1c displays the resulting oscillation of the mean of the normalized population difference $z \equiv (N_L - N_R)/N_t$ as a function of the phase accumulation time t_ϕ , where N_L and N_R are the populations of the left and right wells, respectively, and $N_t \equiv N_L + N_R$.

In the following, we will discuss each step of the sequence in more detail. We first focus on the BEC splitter and find that the state generated inside the interferometer is characterized by a spin-squeezing factor $\xi_S^2 = -7.8 \pm 0.8 \text{ dB}$ (ref. 31), implying that it is entangled³⁹. We then turn to the phase accumulation stage and analyse the phase diffusion process. We find a threefold extension of the coherence time using a number-squeezed state inside the interferometer as compared with a coherent state. Finally, we introduce the non-adiabatic recombiner, and discuss the obtained sensitivity and possible improvements.

Matter-wave source. The experimental sequence starts with a degenerate gas of ^{87}Rb atoms in the $F=1$ hyperfine state in an elongated magnetic trap created by our atom chip setup (cf. Methods)⁴⁰. Using radio-frequency (rf) evaporative cooling, we prepare samples containing $N \equiv \langle N_t \rangle = 1,200$ atoms at a temperature of $T \simeq 20 \text{ nK} = h/k_B \times 420 \text{ Hz}$ and a chemical potential of $\mu/h \simeq 500 \text{ Hz}$, k_B being Boltzmann's constant and h Planck's constant. The brackets denote ensemble averaging. Given the elongated trap geometry, the cloud is in the one-dimensional quasi-condensate regime⁴¹ (cf. Supplementary Note 5).

Splitting. The entire interferometer sequence relies on rf dressing^{42,43} to dynamically turn the static magnetic trap into a double-well potential, whose spacing, barrier height and tilt can be controlled by changing the amplitude and orientation of the rf field. Splitting is performed by increasing the rf amplitude in the dressing wires linearly within 5 ms to transform the single trap into a symmetric double-well potential¹⁹. Along the horizontal splitting direction, the potential has two minima separated by $2 \mu\text{m}$, the barrier height is $h \times 3.7 \text{ kHz}$ and tunnelling is negligible (cf. Methods).

To characterize the quantum state obtained after splitting, we measure the distributions of the two observables atom number difference $n \equiv N_L - N_R$ and relative phase $\phi \equiv \phi_R - \phi_L$. The interferometric sequence can be interrupted at any time to measure these quantities using destructive time-of-flight imaging (see Methods). The relative phase obtained from the Fourier transform of the interference fringes is used to monitor the system during the sequence and must not be confused with the one measured after recombination (measuring the well

populations). Each experimental run gives access to either one or the other observable. We repeat the measurement ~ 200 times to obtain good estimates of both the mean and the variance of n and ϕ .

For non-interacting particles, the atom number difference n is expected to follow a binomial distribution with mean $\langle n \rangle = 0$ and s.d. $\Delta n = \sqrt{N}$ after splitting. As repulsive interactions energetically favour equal populations, reduced fluctuations are expected^{32,44,45}. Figure 2a shows the distribution of detected photon number difference $s \equiv s_L - s_R$ between the left and right clouds (our fluorescence detector registers on average 16 photons per atom, see Methods). Indeed, we observe a suppression of fluctuations by a factor of two compared with shot noise. After correction of the detection noise^{38,46}, we deduce a number-squeezing factor $\xi_N \equiv \Delta n / \sqrt{N} = 0.41 \pm 0.04$ ($\xi_N^2 = -7.8 \pm 0.8 \text{ dB}$). This shows that the splitting process yields a number-squeezed state with reduced fluctuations along one quadrature compared with a classical coherent state.

We now turn to the phase distribution shown in Fig. 2b. As the two variables (ϕ, n) = $2i$) (ref. 31), the Heisenberg uncertainty relation imposes $\Delta\phi \geq 1/\Delta n = 0.074 \text{ rad}$. We observe a Gaussian-shaped phase distribution with vanishing average and

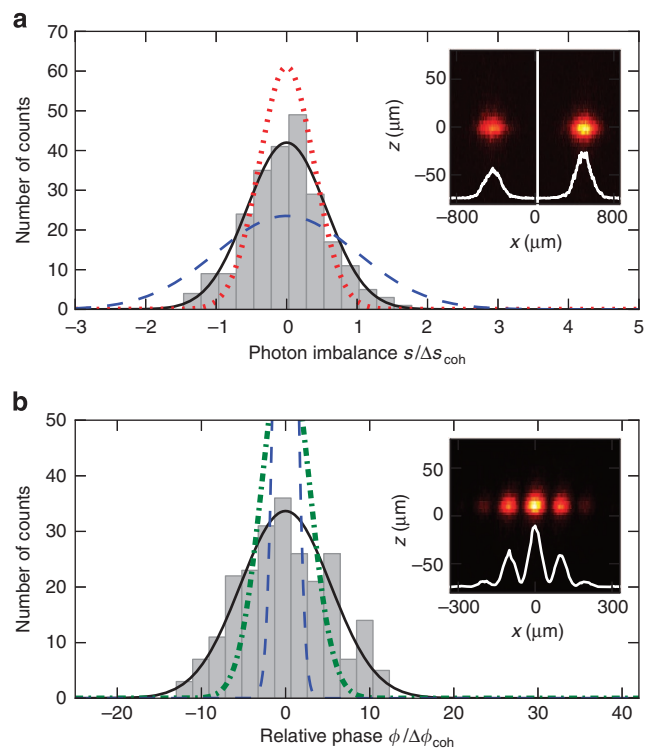


Figure 2 | Number and phase distributions after splitting. (a) Histogram of the difference between the fluorescence signals of the left and right clouds $s = s_L - s_R$, in units of the s.d. expected for a coherent state Δs_{coh} . The curves indicate a normal distribution corresponding to the measured number-squeezing factor $\xi_N = 0.41 \pm 0.04$ (solid black); the distribution expected in the limit $\xi_N = 0$, where only detection noise is responsible for fluctuations (dotted red); and the distribution expected for a coherent state in the absence of detection noise (dashed blue). The inset shows a typical fluorescence picture and the regions used to define s_L and s_R . (b) Histogram of the measured relative phases ϕ in units of the circular s.d. of a coherent state $\Delta\phi_{\text{coh}}$. The curves indicate a normal distribution with the measured s.d. $\Delta\phi = 5.4 \pm 0.5 \times \Delta\phi_{\text{coh}}$ (solid black); and the distributions expected for a coherent state in the absence (dashed blue) and in the presence (dash-dot green) of detection noise. The inset shows a typical matter-wave interference pattern from which the phase is extracted.

circular s.d.⁴⁷ $\Delta\phi = 0.16 \pm 0.01$ rad ($\Delta n\Delta\phi = 2.3$), twice as large as expected from the Heisenberg lower bound. Note that contrary to the number distribution data, the phase distribution data were not corrected for imaging noise. We conjecture that this broadening results from finite initial temperature^{48,49} and detection noise.

Altogether, the output state of the beam splitter exhibits reduced number fluctuations and high coherence properties, characterized by the coherence factor $\langle \cos\phi \rangle = 0.987 \pm 0.001$. It has been shown⁵⁰ that using such a state in an alternative interferometric scheme can allow for a sensitivity better than the standard quantum limit. The improvement in sensitivity is measured by the spin-squeezing factor³¹ $\xi_S \equiv \xi_N / \langle \cos\phi \rangle = 0.41 \pm 0.04$ and corresponds to a gain of 7.8 ± 1 dB over the standard quantum limit. Note that the numerical value of ξ_S is here identical to that of ξ_N , thanks to the large coherence factor of almost unity. Their statistical uncertainties also coincide because that of the coherence factor is negligible compared with that of ξ_N . As spin squeezing, defined as $\xi_S < 1$, is an entanglement witness³⁹, this also demonstrates that our state is non-separable after splitting. The measured fluctuations and coherence imply that our ensemble contains 150 entangled particles in the sense of refs 51,52 and we can exclude entanglement of < 67 atoms with 90% probability.

Phase shifter. We now discuss the phase accumulation stage. After splitting, the coherent superposition of left and right modes has on average $\langle \phi \rangle = 0$ and $\langle n \rangle = 0$. We induce a deterministic shift of the relative phase by tilting the double-well trap out

of the horizontal plane while keeping the well spacing constant. The tilt is performed within 3 ms by modifying the relative current in two rf wires on our atom chip. Given the inter-well distance of $2 \mu\text{m}$ and the angles of $\sim 10^\circ$, this corresponds to velocities at least 30 times smaller than the widths of the velocity distributions of the individual BECs, ensuring that the transfer is sufficiently adiabatic to prevent radial dipole oscillations of the condensates. The tilt is reversed before the recombining sequence. The energy difference ϵ that arises from the tilt (see Supplementary Note 6), triggers a linear evolution of the relative phase given by

$$\phi(t_\phi) = \phi_0 + \epsilon t_\phi / \hbar. \quad (1)$$

In Fig. 3a, the phase evolution is measured for seven different tilt angles ranging from -9° to $+12^\circ$. For these measurements, the phase is obtained directly from interference patterns measured after time-of-flight detection (cf. inset of Fig. 2b). Altogether, this phase accumulation stage acts as a tunable phase shifter for the atomic interferometer. For the fringes presented in Fig. 1c, the angle was fixed to yield the rate $\epsilon/\hbar = -349 \pm 2$ Hz and t_ϕ was varied to tune the phase.

Phase diffusion. In Fig. 3b–e, we observe that the linear evolution of the mean phase discussed above is accompanied by a broadening of the phase distribution, measured by the circular s.d. of the phase $\Delta\phi$ (ref. 47). This phenomenon illustrates phase diffusion²⁶. It corresponds to a dephasing arising from the interactions between the atoms: as the chemical potential of each condensate depends on its atom number, relative number

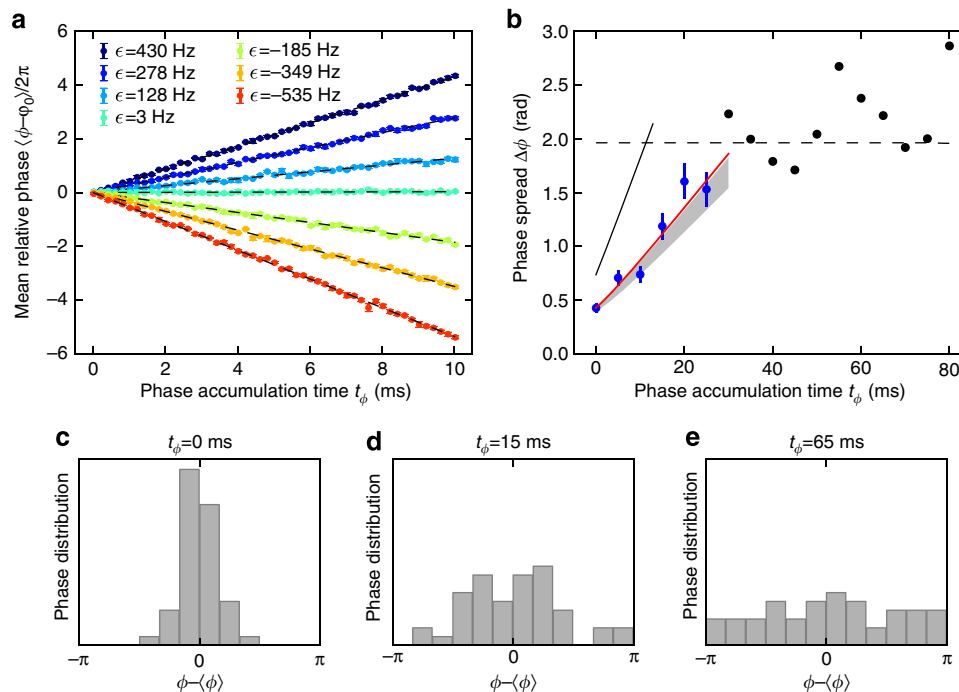


Figure 3 | Evolution of the relative phase and its fluctuations. All data on this figure have been obtained by time-of-flight recombination. **(a)** Linear evolution of the phase for various energy differences ϵ induced by tuning the angle between the two wells. The values of ϵ shown in the legend are obtained from linear fits to the data (black dashed lines). For all fits, the s.e. of the slope is below 3 Hz. The orange points correspond to the rate $\epsilon/\hbar = -349 \pm 2$ Hz used to record the fringes of Fig. 1c. **(b)** Evolution of the circular s.d. of the phase $\Delta\phi$ corresponding to the orange curve of panel a. It exhibits phase diffusion: at short times $t_\phi \lesssim 30$ ms the mean phase is well defined (blue points); on the contrary, for longer times the phase distribution cannot be distinguished from a random distribution (black points, see Methods). The red line is a fit to the blue points with the model of equation (2). Shaded area: theoretical prediction without free parameter, taking into account the measured number squeezing (see text). Black line: expected behaviour if the initial state were classical (that is, not number-squeezed). Note that at $t_\phi = 0$ phase diffusion has already started (see equation (2)). **(c–e)** Measured phase distributions for three values of t_ϕ indicated by the dashed lines. The error bars of a indicate ± 1 circular s.d. divided by $\sqrt{k_i}$, and those of b correspond to ± 1 circular s.d. divided by $\sqrt{2(k_i - 1)}$, k_i being the number of repetition used for each point i .

fluctuations translate into fluctuations of the phase accumulation rate (cf. Supplementary Note 1 for the influence of a residual coupling between the condensates). This leads to an increase of the phase variance given by^{27,28,44}

$$\Delta\phi^2(t_\phi) = \Delta\phi_0^2 + R^2(t_\phi - t_i)^2, \quad (2)$$

where the phase diffusion rate R is

$$R = \frac{\xi_N \sqrt{N}}{\hbar} \left. \frac{\partial \mu}{\partial N} \right|_{N=N/2}, \quad (3)$$

$\mu(N)$ being the chemical potential of one BEC with N atoms. The term $\Delta n = \xi_N \sqrt{N}$ corresponds to the s.d. of the atom number difference n . One sees from equations (3) and (2) that number squeezing, defined as $\xi_N < 1$, reduces phase diffusion and allows longer interrogation times. From a fit (red line in Fig. 3b), we obtain the phase diffusion rate $R = 51 \pm 4 \text{ mrad ms}^{-1}$ and an initial phase spread $\Delta\phi_0 = 300 \pm 90 \text{ mrad}$. The constant $t_i = -6 \text{ ms}$ accounts for the 3 ms used before and after the phase accumulation stage to incline and level the double well.

The measured rate is in fair agreement with the expected value of $R = 46 \pm 4 \text{ mrad ms}^{-1}$ evaluated from equation (3). As the splitting process is not adiabatic with respect to the axial direction, a slow axial quadrupole mode is excited and the condensates are not strictly at equilibrium during phase accumulation. Consequently, the term $\partial\mu/\partial N$ in equation (3) had to be slightly modified to evaluate equation (3) (cf. Supplementary Note 2). This theoretical prediction with no free parameters is represented as a grey shaded area in Fig. 3b. To further confirm our understanding of phase diffusion, we directly measured $\partial\mu/\partial N$ by splitting the initial BEC with an angle leading to a controlled population imbalance, levelling the double well back to horizontal ($\epsilon = 0$), and monitoring the evolution of the phase due to a difference of chemical potential. Together with the squeezing factor and the atom number measured, this gives a third value of $R = 57 \pm 5 \text{ mrad ms}^{-1}$ also in agreement with the two others. For comparison, we evaluate the hypothetical value $R = 112 \text{ mrad ms}^{-1}$ in the absence of number squeezing ($\xi_N = 1$), indicated as a solid black line in Fig. 3b. The difference with our measurements underlines that the interrogation time of our interferometer is extended by the fact that the initial state is number squeezed. Enhanced coherence times have been reported by Jo *et al.*²⁰ and attributed to number squeezing. Our measurement of both number and phase fluctuations corroborates the direct link between phase diffusion and number squeezing.

Recombiner. After the condensates have accumulated a relative phase, the last step consists in recombining the left and right modes in a way that converts the phase into an atom number difference. The recombiner has a role similar to that of the output beam splitter of an optical Mach–Zehnder interferometer. In a two-mode picture, this operation corresponds to a $\pi/2$ pulse. Jo *et al.*²¹ used the phase dependent heating caused by the merging of two condensates to infer the relative phase. It has also been proposed^{23,25} to use a quarter of a Josephson oscillation for this purpose. Nevertheless, one expects the contrast of a Josephson recombiner to be fundamentally limited by the onset of self-trapping when the interaction energy is not negligible compared with the tunnelling energy⁵³. Here, we introduce a different method that makes use of a non-adiabatic transformation of the potential. We abruptly decrease the rf-dressing intensity to reduce the well spacing to $1.5 \mu\text{m}$ and the barrier height to about $h \times 1 \text{ kHz}$ (see Fig. 4a,b). We estimate the energy gap between the two lower-lying single-particle eigenstates of the double-well potential to be $\sim h \times 80 \text{ Hz}$. The clouds are accelerated towards

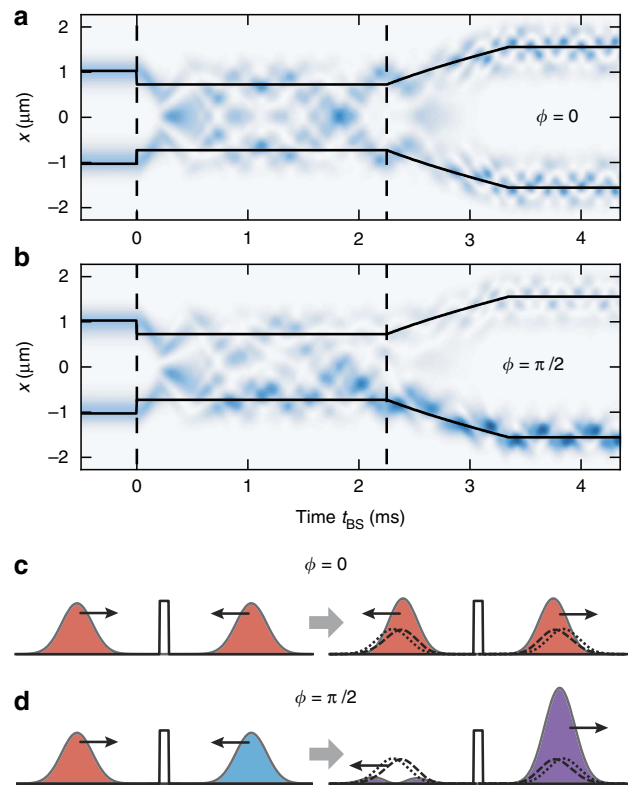


Figure 4 | Principle of the BEC recombiner. (a,b) Numerical simulation of the evolution of the transverse *in situ* density when the double-well spacing is abruptly decreased ($0 < t_{\text{BS}} < 2.25 \text{ ms}$) and increased again ($t_{\text{BS}} > 2.25 \text{ ms}$) for two different initial relative phases: $\phi = 0$ (a) and $\phi = \pi/2$ (b). Black lines: positions of the two potential minima. (c,d) This phase-sensitive recombination can be understood as the propagation and interference of two wave packets launched onto a semi-reflective tunnel barrier. The final wave packets (filled curves with outgoing arrows) are the result of the constructive or destructive interference between the reflected (dashed lines) and transmitted (dotted lines) components arising from the incoming wave packets.

the barrier and, after an adjustable time t_{BS} , the barrier is raised again to separate the atoms for counting. Starting with a state having a phase close to $\pi/2$, we adjusted t_{BS} in order to maximize the final population imbalance. This yielded $t_{\text{BS}} = 2.25 \text{ ms}$. Repeating this operation for different initial phases, we observe the sine-like dependence of the population imbalance shown in Fig. 1c.

This effect can be understood as the splitting of the wave packets on a semi-reflective potential barrier and the interferences between them (Fig. 4c,d). Indeed, in the absence of interactions and assuming two symmetrically incoming wave packets with relative phase ϕ , the linearity of the Schrödinger equation and symmetry of the potential assures that the population difference be given at any time by

$$n(t_{\text{BS}}) = N_i C(t_{\text{BS}}) \sin \phi. \quad (4)$$

The contrast of the read-out $-1 \leq C(t_{\text{BS}}) \leq 1$ depends on the time spent in the coupled double well and is a function of the overlap of the transmitted and reflected modes on each side of the barrier at time t_{BS} (cf. Supplementary Note 3). In a realistic double-well potential, the wave packets undergo a complicated dynamics involving multiple transmissions and reflections, resembling Bragg beams splitters (Fig. 4a,b). Simulations calibrated with the measured trap parameters (see Methods and

Supplementary Note 4) predict a maximum contrast of 80%, limited by the imperfect mode matching in a double well with a finite barrier thickness. Taking into account interactions, no simple analytical model could be found. However, for weak interactions like in our case, numerical simulations yield a sine-like dependence of $n(\phi)$ and up to 70% contrast. Experimentally, we could achieve a contrast of 42% (see below). Possible reasons for this reduction are effects beyond mean field and the coupling to the other spatial directions, both of which are not captured by our simulations.

Interferometric signal. The steps described above are combined to perform the full interferometric sequence depicted in Fig. 1b. Adjusting the phase shifter tilt ϵ/h to -349 Hz, we record the final population imbalance $z = n/N_t$ as a function of the phase accumulation time t_ϕ . For each value of t_ϕ , we typically perform 18 independent measurements of z , and compute the ensemble average and s.d. of $z(t_\phi)$. As expected, we observe that $\langle z \rangle$ oscillates at the frequency ϵ/h . Phase diffusion manifests as a damping of the oscillations associated with increasing fluctuations of z . Note that the error bars of Fig. 1c represent ± 1 s.e.m. For $t_\phi \gtrsim 20$ ms, $\langle z \rangle$ remains close to 0 because of the partial randomization of the phase while single experimental runs can still achieve $\sim 40\%$ imbalance.

To check the consistency of this data with that obtained by time-of-flight recombination (Fig. 3), we derive the expression for $\langle z(t_\phi) \rangle$ at the output of the recombiner. We assume that the relative phase follows a normal distribution with time-dependent mean and variance given, respectively, by equations (1) and (2). Equation (1) describes the phase accumulation while equation (2) accounts for phase diffusion. Assuming that the recombiner acts on the BECs as explained above (cf. equation(4)), we can integrate over the phase distribution to obtain the expression for $\langle z \rangle$ at any time:

$$\langle z(t_\phi) \rangle = C e^{-\Delta\phi_0^2/2} e^{-(Rt_\phi)^2/2} \sin(\varphi_0 + \epsilon t_\phi/\hbar). \quad (5)$$

The initial phase spread is responsible for a reduced contrast of the fringes at $t=0$, while phase diffusion causes a Gaussian damping of the oscillations of $\langle z \rangle$. We set the phase diffusion rate R , the initial phase spread $\Delta\phi_0^2$ and the detuning ϵ to the values obtained from the interference pattern analysis (Fig. 3). The contrast is self-consistently extracted from the data of Fig. 1c by binning all the single-shot population imbalances (Fig. 5) and assuming that ϕ samples the interval $[0, 2\pi]$ uniformly. In the absence of noise, the probability density function of z is given by

$$f(z) = \frac{1}{\pi} \frac{1}{\sqrt{1 - (z/C)^2}} \quad (6)$$

for $|z| < C$, and 0 elsewhere.

To account for technical noise of the Mach-Zehnder interferometer, equation (6) is convolved with a Gaussian function of mean 0 and s.d. σ_z (ref. 54). A fit to the data (red curve of Fig. 5) gives the values of $C = 0.42$ and $\sigma_z = 0.075$.

Equation (5) is used as a fit model for the mean population imbalance of Fig. 1c (solid red line) with only free parameters φ_0 and a constant offset to account for imperfect balancing of the double well. From the technical noise and the contrast extracted from the data of Fig. 5, we estimate the noise on the phase estimation of the non-adiabatic recombiner as $\delta\phi = \Delta n / |\partial n / \partial \phi|_{\phi=0} \simeq \sigma_z / C \simeq 0.18$ rad.

The good agreement of the model with the measurement confirms that the interrogation time of our interferometer is limited exclusively by phase diffusion. The black line in Fig. 1c is the signal expected in the absence of number squeezing. It underlines that the interrogation time is extended by the use of a number-squeezed state.

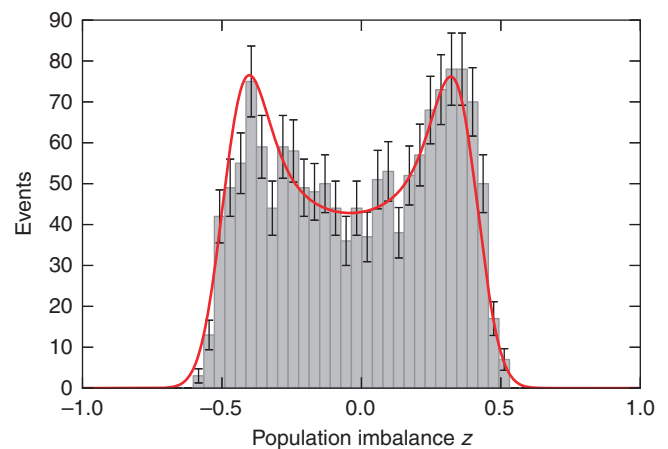


Figure 5 | Distribution of the population imbalance. Histogram of the single-run population imbalance z (grey dots of Fig. 1c). It exhibits the characteristic double structure expected from sampling the sine of a uniformly distributed phase. The contrast and the noise of the recombiner are estimated from convolving the probability distribution function given in equation (6) with a Gaussian noise (red curve). The error bars represent $\pm \sqrt{k_i}$, where k_i is the number of events in the bin of index i .

Discussion

We can now compare the phase-estimation performance of our non-adiabatic recombiner to that of the usual time-of-flight recombination scheme. The intrinsic read-out noise of the non-adiabatic recombiner $\delta\phi = 0.18$ rad is about twice the detection noise of time-of-flight recombination $\delta\phi_d = 0.07$ rad (see Methods). This difference is essentially due to the moderate contrast (42%) of the non-adiabatic recombiner. Were it increased to 100%, for instance through optimal control of the double-well potential^{25,55,56}, the sensitivity of the non-adiabatic recombiner would compete with that of the time-of-flight technique.

We also underline that phase estimation based on atom counting is more robust than phase extraction from interference patterns. First, it does not require high imaging resolution; second, using a recombiner to convert the relative phase into a population imbalance allows the use of the precise atom counting techniques already available^{32,36,38}. Contrary to fringe fitting, it does not rely on time of flight, which makes it more suitable for a fully integrated device on a chip⁵⁷.

A more fundamental distinction between both methods is their potential sensitivity limits. Even though phase estimation based on a fit to the time-of-flight interference pattern can reach sub-shot-noise sensitivity, that is $\delta\phi_{\text{fit}} \leq \delta\phi_{\text{SQL}} \propto 1/\sqrt{N}$, it is fundamentally bounded by $N^{-2/3}$ (ref. 58). This lower bound holds for any entangled state used in the interferometer. This non-trivial result underlines that the Heisenberg scaling of the phase sensitivity $\delta\phi \propto 1/N$ will not be accessible to atom interferometers using this phase-estimation strategy. On the contrary, our non-adiabatic recombiner essentially works as a conventional optical beam splitter, and we thus conjecture that it can reach the Heisenberg scaling^{23,25}.

In conclusion, we have developed a new interferometry technique for trapped and spatially separated BECs based on a novel, non-adiabatic recombiner. The geometry is reminiscent of the familiar optical Mach-Zehnder interferometer. As its two arms are spatially separated, our device is sensitive to differentially applied forces. The tight confinement and precise positioning on an atom chip allows for local probing. We have demonstrated that using a number-squeezed state helps increasing the coherence time, which in turn is still limited to ~ 30 ms by dephasing owing to interactions.

Our observations illustrate a fundamental limitation of interferometry with trapped BECs for precision measurements: interactions dominate the randomization of the phase. This is in contrast to previous experiments, in which technical fluctuations of the energy difference or parasitic excitations during splitting were the dominant cause of dephasing^{18,19}.

Strategies for creating optimal input states, for example, by means of optimal control of the double well, will improve upon our present interferometer only marginally²⁴. To go far beyond requires, in addition, phase-estimation protocols based on Bayesian analysis of the full atom number distribution after the recombiner²⁵. Developing these techniques could yield both a sub-shot-noise sensitivity and a long interrogation time, even in the presence of interactions.

The non-adiabatic recombiner can also be seen as a new tool to perform rotations of the pseudo-spin describing the many-body wave function²³ around the x axis of the Bloch sphere. Such a tool was missing for condensates trapped in double-well potentials. This may prove useful for the tomography of the many-body wave function, for example, to investigate strongly entangled states such as squeezed or Schrödinger cat states.

Methods

Preparation of the condensate. To minimize breathing oscillations during splitting, we prepare the initial quasi condensate in a rf-dressed trap. The rf amplitude is slightly below the splitting threshold⁴². The potential is harmonic along the longitudinal (z) and vertical (y) directions, with trapping frequencies $\nu_z = 12.4$ Hz and $\nu_y = 1.75$ kHz, respectively (see Fig. 1a for the orientation of the axes). In the horizontal, slightly anharmonic direction (x), simulations predict a spacing between the ground and first excited state of 1.02 kHz. By means of rf-evaporative cooling, we prepare samples with <10% relative number fluctuations from shot to shot. The temperature is estimated from the density profile after time of flight using a stochastic model for phase-fluctuating quasi condensates⁵⁹.

Rf dressing. The rf signal is sent through two wires that are parallel to the main trapping wire⁴⁰ (cf. Fig. 1a). In order to turn the trap into a double-well potential, the frequency of the rf field is kept constant 30 kHz below the atomic Larmor frequency of 910 kHz owing to the static fields ($m_F = 0 \rightarrow m_F = \pm 1$ transitions), while the amplitudes in the two wires are ramped up to 52 mA peak to peak, creating an oscillating magnetic field of 1.7 G at the position of the atoms^{19, 42}. The distance between the wells can be tuned by changing the total rf intensity. To tilt the double well, the intensities in the rf wires are varied independently from each other.

Splitting. The double-well potential obtained after splitting is characterized by the trap frequencies of each individual well $\nu_z = 13.2$ Hz and $\nu_y = 1.84$ kHz. Along the splitting direction, we measure for each well $\nu_x = 1.44$ kHz. The two minima are separated by 2 μm and simulations predict a barrier height of $h \times 3.7$ kHz and a tunnel coupling energy of $h \times 0.1$ Hz (ref. 53).

Calibration of the trap simulations. We compute the geometry of the rf-dressed potential beyond the rotating-wave approximation by means of a Floquet analysis⁶⁰. The trap is first simulated from the knowledge of the chip design (Fig. 1a) and the values of the control parameters. The latter are then adjusted in the simulation through independent measurements of the trap properties as follows: for the non-dressed trap, we measure precisely the current in the trap wire and the current in the wires responsible for the longitudinal confinement. This leaves two free parameters to fully define the static trap: the magnetic field B_0 at the centre of the trap and the bias field B_z , which are adjusted to match the measured atomic Larmor frequency and the measured transverse trap frequency. For the rf-dressed trap, the absolute amplitudes of the rf current in each dressing wire are calibrated independently by measuring the trap bottom with one wire at a time. Then both wires are switched on and the relative phase between the rf currents is fine-tuned for the trap bottom of the dressed trap to match the simulation for different values of the global rf intensity. The good agreement of the simulation with the experiment is checked by measuring the distance between the wells (from the fringe spacing of the interference patterns) and the trap frequencies. Furthermore, measurements of the frequency of Josephson oscillations in strongly coupled double wells confirm the good calibration of the trap simulation used, for example, to simulate the recombiner.

Time-of-flight number and phase measurement. At each point in the sequence, we can measure the relative phase and the atom number difference between the

two condensates. To measure the phase, we abruptly switch off the trap, let the clouds overlap and image the interference pattern after 46 ms of free expansion using our light-sheet fluorescence detection system³⁸. We extract the phase from the Fourier transform of the transverse density profile after integration along the longitudinal axis. As the atoms are projected onto the three Zeeman sublevels of the $F = 1$ manifold at switch-off, and to avoid the smearing of the interference patterns inevitably caused by stray fields, a magnetic gradient is applied during time of flight to separate the clouds. The Fourier analysis is performed only on the atoms in $m_F = 0$ (more than half of the total atom number).

Two different methods were used to access the atom number difference $n = N_L - N_R$. For the data of Fig. 2a, the dressing intensity was suddenly raised to increase the splitting distance and give opposite momenta to both clouds. For the data of Fig. 1c, the rf dressing intensity was quickly ramped down to initiate a transverse inward motion in the static harmonic potential. After the atoms acquired a sufficient velocity, the trap was switched off and the two clouds crossed and spatially separated. In both cases, we ended up with two well-separated clouds after time of flight, from which we count the fluorescence photons in regions of equal size.

Number distribution analysis. To measure the atom number difference distribution, we performed the same analysis as Bücke *et al.*⁴⁶ Assuming that the number of fluorescence photons detected from each atom is a random variable of mean p and variance σ_p^2 , and including a random background of variance σ_b^2 , the variance of the photon number difference between the two counting areas is

$$\Delta s^2 = p^2 \xi_N^2 N + N \sigma_p^2 + \sigma_b^2, \quad (7)$$

where $\xi_N = \Delta n / \sqrt{N}$ is the number-squeezing factor. For our detector, the mean of the photon number distribution is $p = 16 \pm 1$ photons per atom. Photon shot noise and the amplification noise of the EMCCD camera yield $\sigma_p^2 = 2p$. Using more than 200 fluorescence pictures to measure Δs^2 and σ_b^2 , we get the value $\xi_N = 0.41 \pm 0.04$ (without correcting for imaging noise, we measure $\xi_{N,\text{unc}} = 0.52$). Setting $\xi_N = 0$ in equation (7) allows to estimate the detection noise (dotted red curve in Fig. 2a).

Phase distribution analysis. To compare the phase distribution measured in Fig. 2b with the one expected from a coherent state, we simulated the full-phase extraction method. We first computed the one-body density distribution corresponding to the ballistic expansion of a symmetric superposition with $\phi = 0$, and generated the positions of the atoms for each realization by drawing N_{tof} independent atom positions from this distribution. As each atom is drawn independently, this procedure mimics a coherent state. We used $N_{\text{tof}} = 500$ to take into account the reduction of the number of atoms we extracted the phase from owing to the Stern–Gerlach separation during time of flight. Taking into account the photon shot noise, the amplification noise of the CCD camera and the optical resolution of our imaging system (we modelled the optical point-spread function by a Gaussian with RMS width of 10 μm , to be compared with the fringe spacing of 107 μm), we produced a large number of interference patterns ($\sim 1,000$), on which we ran our Fourier phase extraction routine. We obtained a Gaussian phase distribution with s.d. $\delta\phi_{\text{tof}} = 0.08$ rad (dot-dash green curve of Fig. 2b), significantly larger than the shot-noise limit expected for an ideal detection system $\delta\phi_{\text{SQL}} = 1/\sqrt{N} \simeq 0.03$ (dashed blue curve).

A rough estimate of the phase detection noise is given by $\delta\phi_d = (\delta\phi_{\text{tof}}^2 - \delta\phi_{\text{SQL}}^2)^{1/2} \simeq 0.07$ rad, showing that detection noise dominates over projection noise.

Test of uniform phase. In Fig. 3b we used a Rayleigh non-uniformity test⁴⁷ to distinguish the points having a uniform phase distribution (black points) from the others (blue points). The blue points correspond to distributions whose P -values were below 0.05, indicating a probability <5% to be compatible with a uniform distribution. Only those points were fitted with equation (2).

Uncertainties and error bars. The uncertainties given in the text, as in $\Delta\phi = 0.16 \pm 0.01$ rad or $\xi_N^2 = -7.8 \pm 0.8$ dB, are statistical uncertainties calculated as follows: for directly measured quantities they are the s.e.m. assuming Gaussian distributions, for fitted parameters we use the s.e. obtained from the fit and for calculated values we use usual error propagation methods.

References

1. Cronin, A. D., Schmiedmayer, J. & Pritchard, D. E. Optics and interferometry with atoms and molecules. *Rev. Mod. Phys.* **81**, 1051–1129 (2009).
2. Ekstrom, C., Schmiedmayer, J., Chapman, M., Hammond, T. & Pritchard, D. Measurement of the electric polarizability of sodium with an atom interferometer. *Phys. Rev. A* **51**, 3883–3888 (1995).
3. Hofferberth, S. *et al.* Probing quantum and thermal noise in an interacting many-body system. *Nat. Phys.* **4**, 489–495 (2008).
4. Gring, M. *et al.* Relaxation and prethermalization in an isolated quantum system. *Science* **337**, 1318–1322 (2012).

5. Weiss, D., Young, B. & Chu, S. Precision measurement of the photon recoil of an atom using atomic interferometry. *Phys. Rev. Lett.* **70**, 2706–2709 (1993).
6. Clauser, J. F. Ultra-high sensitivity accelerometers and gyroscopes using neutral atom matter-wave interferometry. *Physica B* **151**, 262–272 (1988).
7. Peters, A., Chung, K. Y. & Chu, S. Measurement of gravitational acceleration by dropping atoms. *Nature* **400**, 849–852 (1999).
8. Gustavsson, T. L., Landragin, A. & Kasevich, M. A. Rotation sensing with a dual atom-interferometer Sagnac gyroscope. *Classical and Quantum Gravity* **17**, 2385–2398 (2000).
9. Fixler, J. B., Foster, G. T., McGuirk, J. M. & Kasevich, M. A. Atom interferometer measurement of the Newtonian constant of gravity. *Science* **315**, 74–77 (2007).
10. Carusotto, I., Pitaevskii, L., Stringari, S., Modugno, G. & Inguscio, M. Sensitive measurement of forces at the micron scale using Bloch oscillations of ultracold atoms. *Phys. Rev. Lett.* **95**, 093202 (2005).
11. Andrews, M. R. *et al.* Observation of interference between two Bose condensates. *Science* **275**, 637–641 (1997).
12. Hagley, E. W. *et al.* Measurement of the coherence of a Bose-Einstein condensate. *Phys. Rev. Lett.* **83**, 3112–3115 (1999).
13. Bloch, I., Hängsch, T. & Esslinger, T. Measurement of the spatial coherence of a trapped Bose gas at the phase transition. *Nature* **403**, 166–170 (2000).
14. Perrin, A. *et al.* Hanbury Brown and Twiss correlations across the Bose-Einstein condensation threshold. *Nat. Phys.* **8**, 195–198 (2012).
15. Wang, Y.-J. *et al.* Atom Michelson interferometer on a chip using a Bose-Einstein condensate. *Phys. Rev. Lett.* **94**, 090405 (2005).
16. McDonald, G. D. *et al.* Optically guided linear Mach-Zehnder atom interferometer. *Phys. Rev. A* **87**, 013632 (2013).
17. Müntinga, H. *et al.* Interferometry with Bose-Einstein condensates in microgravity. *Phys. Rev. Lett.* **110**, 093602 (2013).
18. Shin, Y. *et al.* Atom interferometry with Bose-Einstein condensates in a double-well potential. *Phys. Rev. Lett.* **92**, 050405 (2004).
19. Schumm, T. *et al.* Matter-wave interferometry in a double well on an atom chip. *Nat. Phys.* **1**, 57–62 (2005).
20. Jo, G.-B. *et al.* Long phase coherence time and number squeezing of two Bose-Einstein condensates on an atom chip. *Phys. Rev. Lett.* **98**, 030407 (2007).
21. Jo, G.-B. *et al.* Phase-sensitive recombination of two Bose-Einstein condensates on an atom chip. *Phys. Rev. Lett.* **98**, 180401 (2007).
22. Baumgärtner, F. *et al.* Measuring energy differences by BEC interferometry on a chip. *Phys. Rev. Lett.* **105**, 243003 (2010).
23. Pezzé, L., Collins, L., Smerzi, A., Berman, G. & Bishop, A. Sub-shot-noise phase sensitivity with a Bose-Einstein condensate Mach-Zehnder interferometer. *Phys. Rev. A* **72**, 043612 (2005).
24. Grond, J., Hohenester, U., Mazets, I. & Schmiedmayer, J. Atom interferometry with trapped Bose-Einstein condensates: impact of atom-atom interactions. *New J. Phys.* **12**, 065036 (2010).
25. Grond, J., Hohenester, U., Schmiedmayer, J. & Smerzi, A. Mach-Zehnder interferometry with interacting trapped Bose-Einstein condensates. *Phys. Rev. A* **84**, 023619 (2011).
26. Lewenstein, M. & You, L. Quantum phase diffusion of a Bose-Einstein condensate. *Phys. Rev. Lett.* **77**, 3489–3493 (1996).
27. Castin, Y. & Dalibard, J. Relative phase of two Bose-Einstein condensates. *Phys. Rev. A* **55**, 4330–4337 (1997).
28. Javanainen, J. & Wilkens, M. Phase and phase diffusion of a split Bose-Einstein condensate. *Phys. Rev. Lett.* **78**, 4675–4678 (1997).
29. Fattori, M. *et al.* Atom interferometry with a weakly interacting Bose-Einstein condensate. *Phys. Rev. Lett.* **100**, 080405 (2008).
30. Gustavsson, M. *et al.* Control of interaction-induced dephasing of Bloch oscillations. *Phys. Rev. Lett.* **100**, 080404 (2008).
31. Kitagawa, M. & Ueda, M. Squeezed spin states. *Phys. Rev. A* **47**, 5138–5143 (1993).
32. Estève, J., Gross, C., Weller, A., Giovanazzi, S. & Oberthaler, M. K. Squeezing and entanglement in a Bose-Einstein condensate. *Nature* **455**, 1216–1219 (2008).
33. Gross, C., Zibold, T., Nicklas, E., Estève, J. & Oberthaler, M. K. Nonlinear atom interferometer surpasses classical precision limit. *Nature* **464**, 1165–1169 (2010).
34. Riedel, M. F. *et al.* Atom-chip-based generation of entanglement for quantum metrology. *Nature* **464**, 1170–1173 (2010).
35. Gross, C. *et al.* Atomic homodyne detection of continuous-variable entangled twin-atom states. *Nature* **480**, 219–223 (2011).
36. Lücke, B. *et al.* Twin matter waves for interferometry beyond the classical limit. *Science* **334**, 773–776 (2011).
37. Hamley, C. D., Gerving, C. S., Hoang, T. M., Bookjans, E. M. & Chapman, M. S. Spin-nematic squeezed vacuum in a quantum gas. *Nat. Phys.* **8**, 305–308 (2012).
38. Bücke, R. *et al.* Single-particle-sensitive imaging of freely propagating ultracold atoms. *New J. Phys.* **11**, 103039 (2009).
39. Sorensen, A., Duan, L. M., Cirac, J. I. & Zoller, P. Many-particle entanglement with Bose-Einstein condensates. *Nature* **409**, 63–66 (2001).
40. Trinker, M. *et al.* Multilayer atom chips for versatile atom micromanipulation. *Appl. Phys. Lett.* **92**, 254102 (2008).
41. Petrov, D., Shlyapnikov, G. & Walraven, J. Regimes of quantum degeneracy in trapped 1D gases. *Phys. Rev. Lett.* **85**, 3745–3749 (2000).
42. Lesanovsky, I. *et al.* Adiabatic radio-frequency potentials for the coherent manipulation of matter waves. *Phys. Rev. A* **73**, 033619 (2006).
43. Hofferberth, S., Lesanovsky, I., Fischer, B., Verdu, J. & Schmiedmayer, J. Radiofrequency-dressed-state potentials for neutral atoms. *Nat. Phys.* **2**, 710–716 (2006).
44. Leggett, A. & Sols, F. Comment on “Phase and Phase Diffusion of a Split Bose-Einstein Condensate”. *Phys. Rev. Lett.* **81**, 1344–1344 (1998).
45. Maussang, K. *et al.* Enhanced and reduced atom number fluctuations in a BEC splitter. *Phys. Rev. Lett.* **105**, 080403 (2010).
46. Bücke, R. *et al.* Twin-atom beams. *Nat. Phys.* **7**, 608–611 (2011).
47. Fisher, N. I. *Statistical Analysis of Circular Data* (Cambridge University Press, 1995).
48. Pitaevskii, L. & Stringari, S. Thermal vs quantum decoherence in double well trapped Bose-Einstein condensates. *Phys. Rev. Lett.* **87**, 180402 (2001).
49. Gati, R., Hemmerling, B., Fölling, J., Albiez, M. & Oberthaler, M. K. Noise thermometry with two weakly coupled Bose-Einstein condensates. *Phys. Rev. Lett.* **96**, 130404 (2006).
50. Wineland, D., Bollinger, J., Itano, W. & Heinzen, D. Squeezed atomic states and projection noise in spectroscopy. *Phys. Rev. A* **50**, 67–88 (1994).
51. Sørensen, A. S. & Mølmer, K. Entanglement and extreme spin squeezing. *Phys. Rev. Lett.* **86**, 4431–4434 (2001).
52. Hyllus, P., Pezzé, L., Smerzi, A. & Tóth, G. Entanglement and extreme spin squeezing for a fluctuating number of indistinguishable particles. *Phys. Rev. A* **86**, 012337 (2012).
53. Raghavan, S., Smerzi, A., Fantoni, S. & Shenoy, S. Coherent oscillations between two weakly coupled Bose-Einstein condensates: Josephson effects, π oscillations, and macroscopic quantum self-trapping. *Phys. Rev. A* **59**, 620–633 (1999).
54. Geiger, R. *et al.* Detecting inertial effects with airborne matter-wave interferometry. *Nat. Commun.* **2**, 474 (2011).
55. Grond, J., Schmiedmayer, J. & Hohenester, U. Optimizing number squeezing when splitting a mesoscopic condensate. *Phys. Rev. A* **79**, 021603(R) (2009).
56. Grond, J., von Winckel, G., Schmiedmayer, J. & Hohenester, U. Optimal control of number squeezing in trapped Bose-Einstein condensates. *Phys. Rev. A* **80**, 053625 (2009).
57. Heine, D. *et al.* A single-atom detector integrated on an atom chip: fabrication, characterization and application. *New J. Phys.* **12**, 095005 (2010).
58. Chwedeńczuk, J., Hyllus, P., Piazza, F. & Smerzi, A. Sub-shot-noise interferometry from measurements of the one-body density. *New J. Phys.* **14**, 093001 (2012).
59. Stimming, H.-P., Mauser, N., Schmiedmayer, J. & Mazets, I. Fluctuations and stochastic processes in one-dimensional many-body quantum systems. *Phys. Rev. Lett.* **105**, 015301 (2010).
60. Hofferberth, S., Fischer, B., Schumm, T., Schmiedmayer, J. & Lesanovsky, I. Ultracold atoms in radio-frequency dressed potentials beyond the rotating-wave approximation. *Phys. Rev. A* **76**, 013401 (2007).

Acknowledgements

We are grateful to Thomas Betz, Stephanie Manz and Aurélien Perrin for earlier work on the experiment. We thank Igor Mazets, Remi Geiger, Jan Chwedeńczuk and Patrizia Vignolo for helpful discussions. J.-F.S. acknowledges the support of the Austrian Science Fund (FWF) through his Lise Meitner fellowship (M 1454-N27). T.B. and R.B. acknowledge the support of the Vienna Doctoral Program on Complex Quantum Systems (CoQuS). This research was supported by the European STREP project QIBEC (284584), the European Integrated project AQUITE (247687) and the FWF projects SFB FoQuS (SFB F40) and CAP (I607-N16).

Author contributions

T.B. and J.-F.S. performed the experiments and analysed the data. S.v.F., T.B. and J.-F.S. performed numerical simulations. All the authors contributed to the elaboration of the experiment and to the final manuscript.

Additional information

Supplementary Information accompanies this paper at <http://www.nature.com/naturecommunications>

Competing financial interests: The authors declare no competing financial interests.

Reprints and permission information is available online at <http://npg.nature.com/reprintsandpermissions/>

How to cite this article: Berrada, T. *et al.* Integrated Mach-Zehnder interferometer for Bose-Einstein condensates. *Nat. Commun.* **4**:2077 doi: 10.1038/ncomms3077 (2013).



This work is licensed under a Creative Commons Attribution-NonCommercial-ShareAlike 3.0 Unported License. To view a copy of this license, visit <http://creativecommons.org/licenses/by-nc-sa/3.0/>